Rapid enhancement of chemical weathering recorded by extremely light seawater lithium isotopes at the Permian–Triassic boundary

He Sun[a,b], Yilin Xiao[a,1], Yongjun Gao[c,1], Guijie Zhang[a], John F. Casey[c], and Yanan Shen[a,1]

[a]Chinese Academy of Sciences Key Laboratory of Crust-Mantle Materials and Environments, School of Earth and Space Sciences, University of Science and Technology of China, Hefei 230026, China; [b]School of Resources and Environmental Engineering, Hefei University of Technology, Hefei 230009, China; and [c]Department of Earth and Atmospheric Sciences, University of Houston, Houston, TX 77204-5007

Edited by Mark H. Thiemens, University of California, San Diego, La Jolla, CA, and approved February 23, 2018 (received for review July 2, 2017)

Lithium (Li) isotope analyses of sedimentary rocks from the Meishan section in South China reveal extremely light seawater Li isotopic signatures at the Permian–Triassic boundary (PTB), which coincide with the most severe mass extinction in the history of animal life. Using a dynamic seawater lithium box model, we show that the light seawater Li isotopic signatures can be best explained by a significant influx of riverine [Li] with light δ^7Li to the ocean realm. The seawater Li isotope excursion started ≥300 Ky before and persisted up to the main extinction event, which is consistent with the eruption time of the Siberian Traps. The eruption of the Siberian Traps exposed an enormous amount of fresh basalt and triggered CO_2 release, rapid global warming, and acid rains, which in turn led to a rapid enhancement of continental weathering. The enhanced continental weathering delivered excessive nutrients to the oceans that could lead to marine eutrophication, anoxia, acidification, and ecological perturbation, ultimately resulting in the end-Permian mass extinction.

end-Permian mass extinction | Li isotopes | Meishan section | continental weathering | Permian–Triassic boundary

The Permian–Triassic boundary (PTB) at ∼251 My marked the most severe mass extinction in the history of animal life, with over 80% of all marine species, ∼70% of terrestrial vertebrate genera, and most land plants eliminated (1–4). The PTB is characterized by a series of abrupt ecosystem changes, such as an increase in atmospheric CO_2 concentration, rapid global warming, terrestrial wildfires, acid rains, ocean acidification, and marine anoxia (3–9). The causes of the extinction are under debate, but have been attributed to causes including massive flood basalt volcanism (Siberian traps), meteorite impact, marine anoxia, and massive methane clathrate dissociation (1, 4–12). All these hypotheses predict a greenhouse event; thus, enhanced chemical weathering at this period may be expected. High Ba/Sr ratios of paleosols from Graphite Peak, Antarctica, support an abrupt increase in chemical weathering in the earliest Triassic in the region (13). Systematic changes in sediment fluxes in the aftermath of the end-Permian crisis and strontium isotope changes across the PTB in condodonts appear to indicate elevated weathering rates in the Early Triassic (14, 15). A promising and newly developed indicator for ancient global weathering rate is represented by paleomarine Li isotopes derived from sedimentary carbonates (16–18). Unlike other isotopic systems such as Sr and Os, Li is almost solely hosted in silicate minerals and is advantageous because it remains insensitive to weathering of continental and marine carbonate (affects Sr isotopes) or black shale (affects Os isotopes) (19, 20). Also, Li isotopes are not fractionated through redox reactions and biological processes (21). Riverine Li signals are exclusively dominated by weathering of silicate rocks; hence they can provide unique information on silicate weathering rate and carbon dioxide consumption during weathering (16–18, 22).

Here, we present lithium isotope analyses, as well as major and trace-element compositions, of bulk rock samples from the Meishan section in South China. We aim to constrain the Late Permian–Early Triassic weathering rate and its potential impact on global climate changes when the end-Permian extinction occurred.

Stratigraphy and Sampling

The Meishan section in South China, as the Global Stratotype Section and Point (GSSP) of the PTB, is one of the most extensively examined sections worldwide with respect to the end-Permian biotic crisis (3, 12, 23, 24). Our samples were collected from the well-documented Late-Permian Changhsing (Beds 22–24) and Early Triassic Yinkeng formations (Beds 25–34) from the Meishan section (Fig. 1). The Meishan section comprises varying lithologies. Beds 22–24 consist of bioclastic to micritic limestones. Bed 25 is a 4-cm-thick, whitish claystone. The base of Bed 25 is uneven and represented by a very thin (∼ 0.3-cm-thick) pyrite lamina. Bed 26 is a 6-cm-thick, dark-gray claystone. At Meishan, the end-Permian extinction preserved by Beds 25–26 is estimated to have marked a loss of ∼94% of marine species (3). Bed 27 consists of light-gray biotic packstone to wackestone with occasionally micrite texture. The index taxon *Hindeodus parvus* first appearing at the base of Bed 27c marks the GSSP of the PTB (23). Bed 28 is gray-green claystone of ∼0.5 cm thickness. Bed 29 is dominated by wackestone and overlain by marlstone up

Significance

Estimates of seawater Li isotopic composition at the Permian–Triassic boundary (PTB) reveal extremely light seawater Li isotopic signatures accompanying the most severe mass extinction in the history of animal life. Theoretical modeling indicates a rapid enhancement of continental weathering during this time, which was likely triggered by the eruption of the Siberian Traps, rapid global warming, and acid rains. Our results provide independent geochemical evidence for an enhanced continental chemical weathering at the PTB, illustrating that continental weathering may provide a key link between terrestrial and marine ecological crises.

Author contributions: Y.X., Y.G., and Y.S. designed research; Y.X., Y.G., and J.F.C. provided laboratory facilities; H.S., Y.X., and Y.G. performed research; H.S. and Y.G. analyzed data; Y.S. and G.Z. provided samples and a stratigraphic framework; and H.S., Y.X., Y.G., G.Z., J.F.C., and Y.S. wrote the paper.

The authors declare no conflict of interest.

This article is a PNAS Direct Submission.

[1]To whom correspondence may be addressed. Email: ylxiao@ustc.edu.cn, yongjungao@uh.edu, or yashen@ustc.edu.cn.

This article contains supporting information online at www.pnas.org/lookup/suppl/doi:10.1073/pnas.1711862115/-/DCSupplemental.

Published online March 26, 2018.

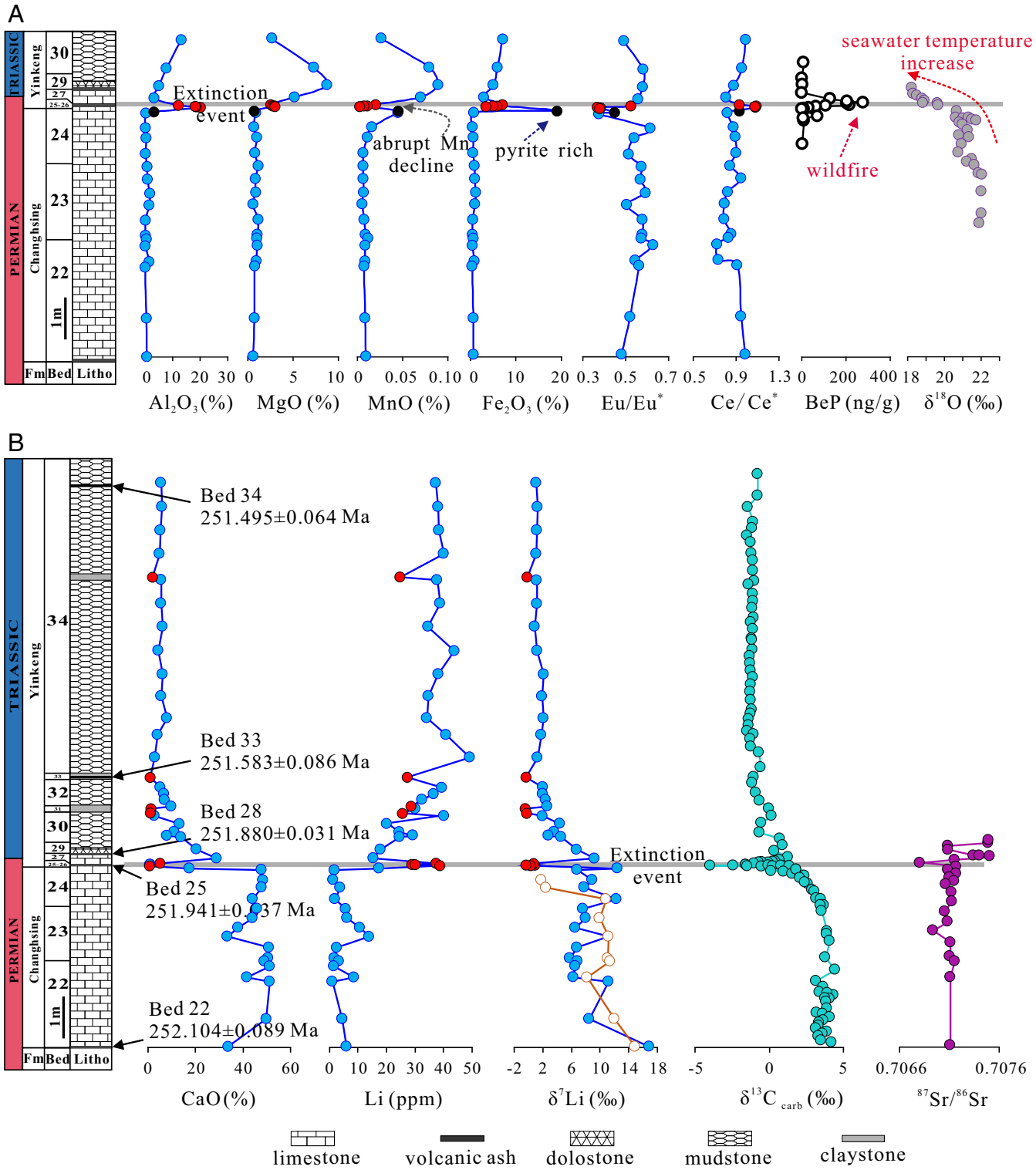

Fig. 1. (*A* and *B*) Stratigraphy, geochronology, major and trace-element concentrations, black carbon (BeP), O isotopes, Li isotopes, Sr isotopes, and carbonate carbon isotopic composition for the Meishan section. Tawny circle in δ^7Li diagram represents analysis of carbonate fractions in limestones through chemical separation method. Claystones layers are marked by red circle. Stratigraphic column of the PTB is revised from ref. 12, ages and carbonate carbon isotopic excursion after ref. 25, black carbon data from ref. 5, O isotope data from ref. 8, and Sr isotope data from ref. 15.

to Bed 34. Beds 30–34 are dominated by organic-rich mudstone and black shale with several claystone layers.

The most up-to-date geochronological U/Pb dating on zircons from volcanic ash beds has yielded minimum detrital ages of 252.104 ± 0.060 My from the stratigraphically older Bed 22, 251.941 ± 0.037 My from Bed 25, 251.880 ± 0.031 My from Bed 28, 251.583 ± 0.086 My from Bed 33, and 251.495 ± 0.064 My from Bed 34 (25). These ages are sequentially

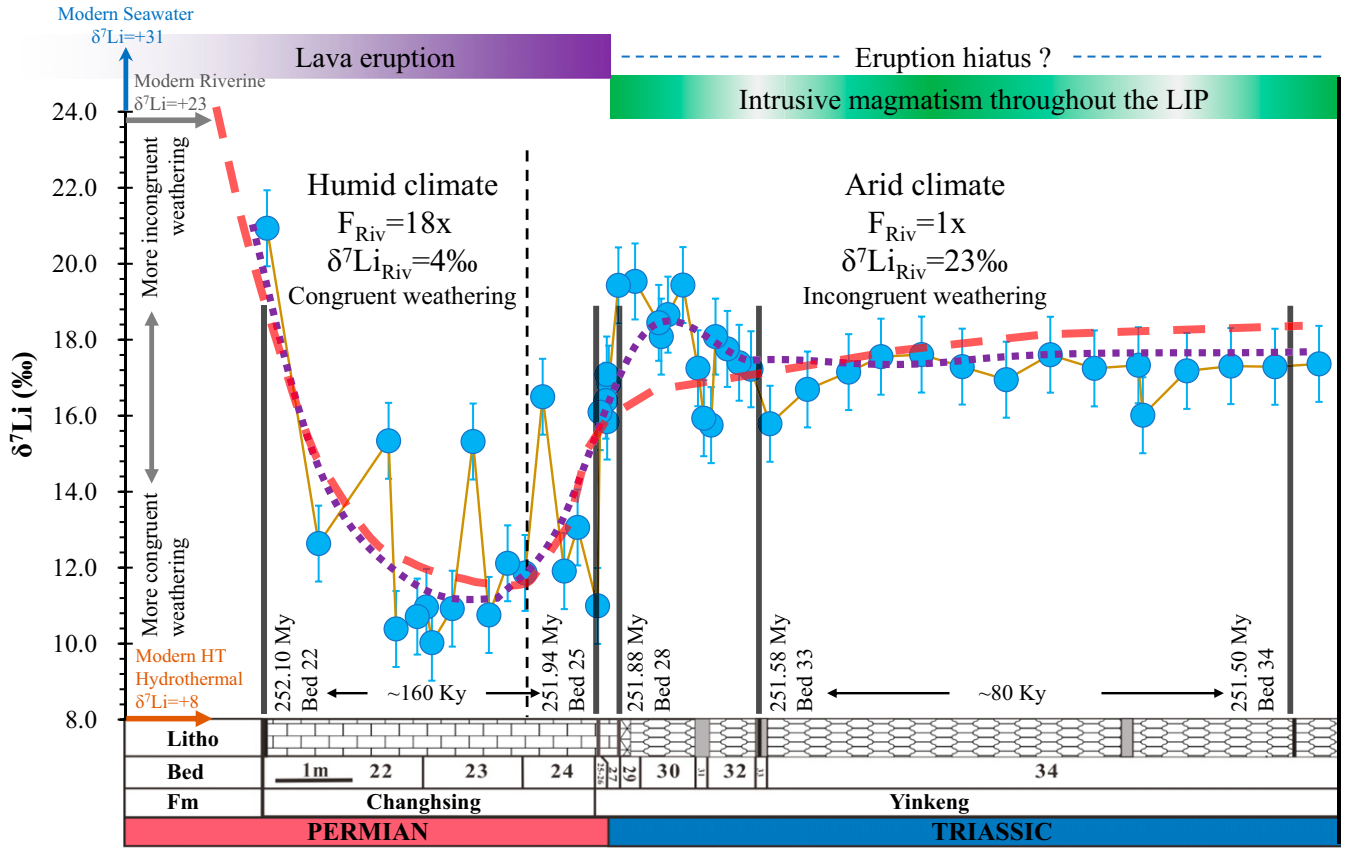

Fig. 2. Seawater δ^7Li at the PTB and dynamic modeling fit to the observed data. Model line (red dashed line) represents the variation of lithium isotope composition of seawater corresponding to enhanced weathering pulse (with 18× Li flux and δ^7Li ~4‰) started before Beds 22–23 for ~300 Ky and subsequent decrease in weathering rate (with 1× Li flux and δ^7Li ~23‰) from Bed 24 to Bed 34 for ~400 Ky. Purple dotted line is the smoothed seawater Li isotopic trend. Detailed modeling parameters can be found in *SI Appendix*, Table S3. The modeling suggests climate change from humid to arid at PTB, which is consistent with the eruption time of the Siberian Traps. Dashed black line corresponding to the early stage of Bed 24 represents the change of modeling parameters. Timeline of Siberian Traps LIP magmatism (purple and green bands) and dated ash beds from the Meishan section (black bars) are from refs. 25 and 46.

younger in a direction and are consistent with U/Pb age dating of volcanic ash layers from terrestrial and deep marine sections, which establish the onset of the Triassic (26, 27).

Major and Trace Element and Li Isotopic Compositions

Bulk rock samples from the Meishan section were measured for major and trace elements and Li isotopes. Both Li concentration and isotopic compositions show large variations across the PTB (Fig. 1). Beds 22–24 show relatively high δ^7Li values from +6.3 to +16.8‰ (mostly from +6 to +12‰), whereas the element concentrations remain at low levels (<10 ppm). δ^7Li values start to decrease at Bed 25 and reach the minimum (−0.3 to +1.0‰) with high Li concentrations (29.0–39.2 ppm) within Beds 25–26, where the negative carbon isotope excursion and well-documented biotic crisis peak have been reported (3). After a brief increase in δ^7Li values and decrease in Li contents (Bed 26 to Bed 27), the progression from Bed 27 to Bed 34 shows systematic decrease from +9.3‰ to +1.0‰ in δ^7Li with variable Li abundance ranging from 15.3 to 49.4 ppm. Claystone layers from Beds 26–34 show uniform light Li isotopic compositions of −0.3‰ to −0.1‰ that resemble Bed 25. Major and trace elements also show variations stratigraphically, with the most notable features being negative Eu/Eu* and positive Ce/Ce* anomalies, and abrupt Mn decline at the PTB (Fig. 1*A*). The carbonate fractions in limestones exhibit similar Li isotopic compositions with the bulk rocks (Fig. 1*B*).

Seawater Li Isotope Reconstruction for the PTB

Given that the residence time of Li in seawater (~1.2 My) is much longer than the oceanic mixing time (~1,000 y) (16), Li in present-day seawater is well mixed vertically as well as laterally homogeneous in both elemental concentration and isotopic composition {$[Li]_{SW}$ = 0.2 ppm; δ^7Li_{SW} = +31‰ (28–30)}. It has also been well documented that the lithium isotopic fractionation between seawater and marine sediments is relatively constant [$\Delta_{SW\text{-biogenic carbonate}}$ ~3–5‰; $\Delta_{SW\text{-clay}}$ ~16–19‰ (28, 31)]. Thus, marine sediment can provide an archive for the ^{7}Li/^{6}Li of contemporary seawater (16, 17, 32).

The sediments from the Meishan section show similar Rare Earth Element patterns to the marine carbonate, indicating that they were marine authigenic sediments (*SI Appendix*, section I). To reconstruct the Li isotopic composition of seawater, [Li]-Al_2O_3, δ^7Li-Al_2O_3, δ^7Li-1/[Li], CaO-1/[Li], and δ^7Li-CaO diagrams were used to evaluate the relative proportion of carbonates and clays in different beds (*SI Appendix*, Figs. S2, S3, and S7–S9). Limestones from Beds 22–24 show strong positively correlated Li and Al_2O_3 contents (*SI Appendix*, Fig. S2), which may be interpreted as resulting from mixing between clay minerals and carbonate. However, the very low Al/Li ratios of ~0.17 (carbonate mixing with clays would result in Al/Li values of ~0.4) and variable δ^7Li, independent of Al content (*SI Appendix*, Fig. S3), rule out this possibility. Carbonate mixing with chert (Al_2O_3 ~3 wt %, [Li] ~20 ppm) is a more likely explanation (33, 34). This interpretation is supported by the [Li]-[B], [Li]-Fe_2O_3 and Pb-Sr

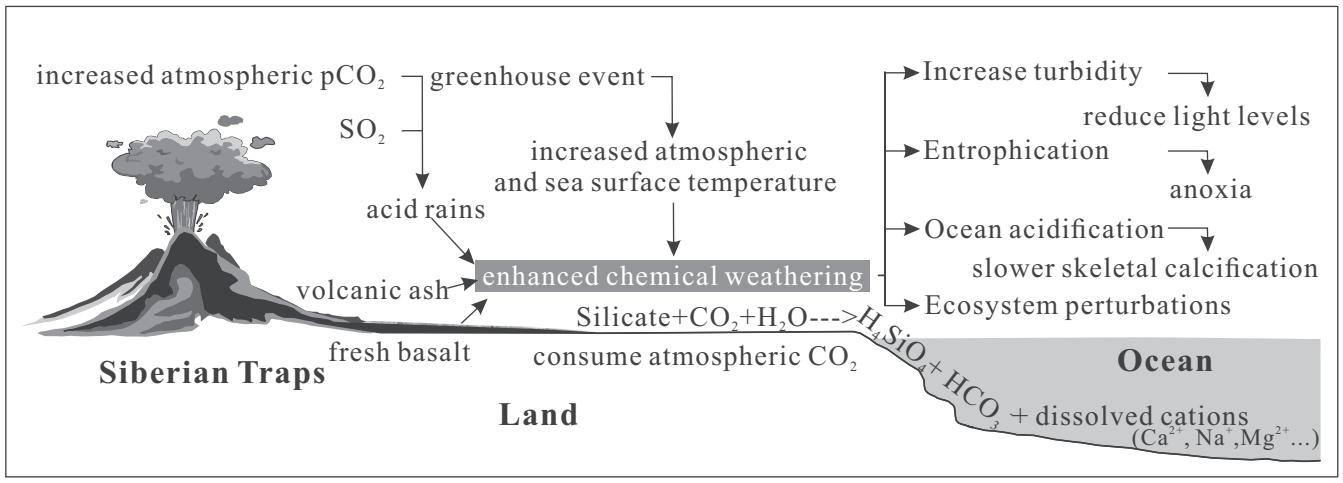

Fig. 3. Schematic model linking the eruption of the Siberian Traps, acid rains, greenhouse event, enhanced global chemical weathering, and their ecological consequences to the marine realm during the Latest Permian. Events are arrayed by cause-and-effect relationships. Note that the continental weathering and riverine nutrient delivery plays a critical role that links terrestrial and marine ecological crises.

data (*SI Appendix*, Figs. S4–S6). Although a fractionation factor in chert is lacking, samples from Beds 22–24 show no linear correlation between δ^7Li with abundance of Li or Al_2O_3. This, and the similar Li isotopic values between the limestones and the carbonate fractions therein (Fig. 1*B*), together with the good correlation between Al_2O_3 and [Li], indicate that chert should have Li isotopic compositions similar to carbonate. These observations imply that without the mixing of clays, the limestones from Beds 22–24 may represent primary seawater signatures by adding a 3–5‰ fractionation (17). Calcareous mudstone samples from Beds 26–34 define mixing trends in δ^7Li-Al_2O_3, [Li]-Al_2O_3, CaO-1/[Li], and δ^7Li-CaO diagrams, with Al_2O_3/Li values of ∼0.4, indicating increased proportions of clays. The well-defined mixing line (1/[Li]-δ^7Li) of Beds 26–34 implies two steady-state end members, carbonates and clays. The mixing calculation yielded δ^7Li values of ∼+11.5‰ for limestones and ∼−0.2‰ for clays. In this way, the estimated Li isotope composition for seawater calculated from both carbonates (∼+14.5–+16.5‰) and clays (∼+15–+18‰) are in good agreement. Bed 25, having high Al_2O_3, B and low Ti, Na, Fe, Co concentrations, is clearly different from other samples. These features could be attributed to high Kaolin proportions in Bed 25, which are documented with the X-ray diffraction data of the Meishan section (35). The high Li, Al, and B (B up to 117 ppm) concentrations imply that clays dominate Li in Bed 25. Estimated seawater Li isotope compositions from Bed 25 is ∼+16.0–+18‰, resembling the values of Beds 26–34. Similar treatment was also applied to the claystones from Beds 26–34, which also yielded coherent seawater Li isotope values of ∼+16‰. Constructed paleo-seawater Li isotope records from the Meishan section are listed in *SI Appendix*, Table S1 and plotted in Fig. 2.

Enhanced Weathering Associated with the End-Permian Mass Extinction

Ancient seawater lithium isotope records are important in documenting continental weathering and paleoclimate changes (16). Estimated δ^7Li values for seawater proximal to the PTB at Meishan range from +10 to +21‰ (mostly +10 to +18‰ except for one relatively high value of +21‰ at the base of Bed 22), which is much lighter on average (∼15‰) than the value of ∼+31‰ for present-day seawater (36). A box model is used here (*SI Appendix*, section I) to constrain the possible origin of low-seawater δ^7Li. Fractionation of isotopes during removal of Li from seawater into clays is assumed to be constant ($\Delta_{SW\text{-}SED}$ ∼ 16‰), because the process of clay mineral formation and alteration of oceanic crust shows little change over time (16, 29). Thus, the main driver of ocean δ^7Li_{SW} change is the input Li fluxes from continental silicate weathering and high-temperature (HT) vent fluids. Modeling suggests that changing of HT flux could lead to Li isotopic shifts. However, if riverine Li stays unchanged, HT (even 20× of present-day flux) alone cannot yield the observed isotopic values at the PTB. Hydrothermal flux is related to seafloor spreading rates, empirically proportional to midocean ridge volume. Based on the low sea level at the end-Permian and the existence of supercontinent Pangea (320–185 My), the ridge volume was probably at a minimum at that time (37). High-resolution Sr isotope records of carbonate show increased $^{87}Sr/^{86}Sr$ at the end-Permian, reflecting either high riverine Sr input or restrained hydrothermal flux (38, 39). These constraints, taken together, imply that the hydrothermal flux at the end-Permian should be less than today and that a more plausible mechanism for the low Li isotope signature in seawater is the change of weathering Li input. Unlike hydrothermal fluid, riverine Li covers a large range of isotopic compositions from ∼+2‰ (congruent weathering) to ∼+42‰ (highly incongruent weathering) (17, 36, 40). Moreover, riverine Li flux, as a function of $[Li]_{river}$ and global water flux, could have been significantly changed with climate variations. A decrease in δ^7Li from +20 to +2‰ with a constant Li river flux for 5 My would result in seawater value changes from +29 to +23‰, which is still much higher than the observed seawater δ^7Li values at the PTB. Thus, modeling the observed low δ^7Li requires an enhanced riverine Li flux accompanied by very light isotopic compositions. Such a process could occur, as intense congruent weathering (high silicate minerals dissolution rate) results in both low δ^7Li and high [Li] in rivers. Further modeling indicates (*SI Appendix*, section I) that if the river δ^7Li is ∼+4‰, the Li flux would have to increase ∼15–18× to yield the observed light seawater δ^7Li (+10–+16‰).

The above discussions suggest that the end-Permian riverine Li exhibits very light isotopic compositions with fluvial flux increasing about 10–18× relative to present day, and thus indicates an enhanced weathering rate. High-precision age dating indicate coincidence of the PTB with the largest igneous-province (LIP) formation on the Earth, the Siberian Traps (41, 42). The LIP exposed an enormous flood basalts province (∼7×10^6 km^2) and

contributed volcanic ash to the Earth's surface. Both would release light Li during chemical weathering (43). Because the dissolution rates of minerals decrease in the order of olivine > Ca-plagioclase > pyroxene > Na-plagioclase > K-feldspar > muscovite > quartz (22), basalts, mainly composed of pyroxene + plagioclase + olivine + glass, would be weathered very rapidly and highly congruent (i.e., few secondary minerals precipitated due to their freshness and aluminum-deficient nature). Volcanic ash, with high reactive surface area during weathering, would result in even higher weathering rate than the basalts (22). Thus, rapid dissolution of the fresh Siberian flood basalts and volcanic ash may have played an important role in the rapid enhancement of chemical weathering rates at the PTB. The massive volcanism has also outgassed large amounts of CO_2 and SO_2 aerosols into the atmosphere (44). This process, together with possible methane clathrate dissociation, may have led to a global warming and acid rain (6, 13, 45). Experimental studies have demonstrated that mineral dissolution under acidic conditions is an order of magnitude faster than dissolution under neutral pH (22). Therefore, it is likely that the extremely enhanced chemical weathering at PTB may have resulted from hot acid rain weathering of fresh erupted basalts.

The coincidence between the extinction event and dramatic climate changes has been shown at the Meishan section. Beds 25–26, with a loss of >90% of marine species within less than 0.5 My, marked the main phase of the PTB mass extinction (3). The main phase of the marine PTB mass extinction occurred synchronously with the sedimentary-ecosystem transition from a humid tropical biota to oolites and calcimicrobialites deposited under arid climate conditions (24). Black carbon, as a proxy of forest wildfire at the PTB, starts to increase in Beds 23–24 and reached a climax in Beds 25–26, reflecting climate transition to arid condition and forest decimation (Fig. 1*A*) (5). Such a climate change should have repressed the weathering rate, and thus might have resulted in decreased riverine Li flux and possibly higher δ^7Li. This is consistent with the elevated seawater δ^7Li in Beds 25–34 (~4‰ higher than Beds 22–24, Fig. 2). Our modeling results indicate that a first enhanced weathering pulse (with 18× Li flux and δ^7Li ~ +4‰) for ~300 Ky and subsequent decrease in weathering rate (with 1× Li flux and δ^7Li ~ +23‰) from Bed 24 to Bed 34 for ~400 Ky fit the best for the measured data (Fig. 2). The modeling cannot provide details to global riverine Li variations, but the data suggest that the estimated seawater δ^7Li values require an initial increase and then a restrained riverine Li input, further validating the possibility of a globally enhanced chemical weathering and climate change from humid to arid conditions at the PTB.

The eruption of the Siberian Traps is widely proposed to have triggered the end-Permian extinction (1). The Eu/Eu* profile of conodont bioapatite shows mantle-sourced values of 1.0–1.5 in Bed 24e, indicating a possible fingerprint of the Siberian Traps eruption (35). Reported high-precision dating of the Siberian traps confirms about two-thirds of the total lava/pyroclastic volume was erupted over ~300 Ky, before and concurrent with the end-Permian mass extinction (46). The eruption of the Siberian Traps exposed enormous fresh basalt as well as volcanic ash onto the continents, and released significant amounts of CO_2 and SO_2 aerosols into the atmosphere, triggered acid rains and greenhouse warming, and ultimately resulted in enhanced global weathering rate with light riverine and seawater δ^7Li as we observed from the Meishan section. Unlike Li isotopes, the high-resolution seawater Sr record indicates high weathering rates which coincide with the PTB interval and the Early Triassic (15). However, by coupling seawater Sr isotope changes and the timing of the Siberian Traps, it is likely that the end-Permian Sr cycle may have been significantly perturbed by the fast weathering of unradiogenic flood basalts. Therefore, Sr isotopes may not be a straightforward tracer of continental weathering for this case given the unradiogenic nature of the Siberian Traps.

Chemical weathering of silicate consumes atmospheric CO_2 and brings HCO_3^-, dissolvable cations (such as Mg^{2+}, Ca^{2+}, Na^+), and suspended matter to the marine system. Hence, a rapid enhancement of chemical weathering would have led to increased riverine nutrient fluxes and elevated turbidity (Fig. 3). It has been proposed that increased sediment fluxes in the Early Triassic may have caused severe biological consequences, such as reducing light levels and photosynthesis, slowing skeletal calcification, depleting dissolved oxygen, and smothering benthic organisms (14). The observed Mn decline, negative Eu/Eu*, and positive Ce/Ce* anomalies at Beds 25–26 support marine anoxia at the time (47). Recent studies revealed that the Cenomanian–Turonian boundary (the Ocean Anoxic Event 2), which was marked by high atmospheric pCO_2, high sea-surface temperature, global marine anoxia, and mass extinction, was also accompanied by enhanced global weathering rates (17). The remarkable light seawater Li isotope reported in this study provides independent geochemical evidence of an enhanced chemical weathering at the PTB. The enhanced continental weathering delivered excessive nutrients to the oceans, leading to marine eutrophication, anoxia, acidification, and ecological perturbation, and may ultimately have led to the end-Permian mass extinction (Fig. 3). Our Li isotopic study of the Meishan section demonstrates that enhanced continental weathering may provide a key link between terrestrial and marine ecological crises, and future Li isotopic investigation on other PTB sections can test the present hypothesis.

Methods

For bulk-rock Li isotope analysis, ~100 mg of bulk-rock powders were completely digested in a 3:1 mixture of double-distilled HF and HNO_3 at 180 °C. The samples were then dried, refluxed three to four times in 8 M HCl, and redissolved in 0.2 M HCl for column purification. For carbonate fraction in limestones, a chemical leaching method using dilute acid was applied (17). Approximately 200 mg of bulk carbonate was leached in 0.1 M HCl for 1 h. After centrifugation, the supernatants were then dried and redissolved in 0.2 M HCl for column purification. Separation of Li for isotopic composition analysis was achieved by an organic solvent-free two-step liquid chromatography procedure in a clean laboratory at the University of Houston (48). Large columns (15 mL first step columns and 5 mL for second step columns) were used to ensure that the column was not saturated for sodium and other cations, which is important for low Li samples. All separations were monitored with quadrupole inductively-coupled plasma mass spectrometer (ICP-MS) analysis to guarantee both high Li yield and low Na/Li ratio (<0.5). Solutions for multicollector inductively coupled plasma mass spectrometry (MC-ICP-MS) analysis were matrix matched to 10 or 50 ppm according to the bracketing standards to ensure the best precision and accuracy. The total procedure blanks determined for the combined sample digestion and column procedure were about 0.03 ng Li. Compared with the ~50–4,500 ng Li used for our analysis, the blank correction is not significant at the uncertainty levels achieved. We report results as $\delta^7\text{Li} = \{[(^7\text{Li}/^6\text{Li})\text{sample}/(^7\text{Li}/^6\text{Li})\text{standard}] - 1\} \times 1{,}000$, relative to the L-SVEC Li-isotope standard (49).The lithium isotopic compositions were analyzed on a high-resolution Nu Plasma II MC-ICP-MS at University of Houston and a Neptune plus MC-ICP-MS at University of Science and Technology of China (50). Aqueous samples were introduced through a Cetac Aridus II desolvating nebulizer. Each sample analysis was bracketed before and after by 10 or 50 ppb international Li isotopic standard (L-SVEC). The in-run precision on ^{7}Li/^{6}Li measurements is ≤0.2‰ for one block of 50 ratios. The external precision, based on 2σ of repeat runs ($n > 10$) of pure Li standard solutions and United States Geological Survey standards, is ≤0.5‰. Analysis of international rock reference materials yields δ^7Li values of +4.29 ± 0.23‰, +3.14 ± 0.41‰, and +4.91 ± 0.34‰ for BHVO-2, JP-1, and DTS-2, respectively.

ACKNOWLEDGMENTS. Fengtai Tong and Haiyang Liu are thanked for assistance with the Li isotope analysis. We appreciate constructive comments from two anonymous reviewers and the editor. We thank Hanjie Wen for providing samples used in this study. This work was financially supported by the Strategic Priority Research Program (B) of the Chinese Academy of Sciences (XDB18000000), the National Natural Science Foundation of China (41673031, 41721002, 41603005, 41473033, 41330102), and the 111 Project.

1. Erwin DH (2006) *Extinction: How Life on Earth Nearly Ended 250 Million Years Ago* (Princeton Univ Press, Princeton), p 296.
2. Stanley SM (2016) Estimates of the magnitudes of major marine mass extinctions in earth history. *Proc Natl Acad Sci USA* 113:E6325–E6334.
3. Jin YG, et al. (2000) Pattern of marine mass extinction near the Permian-Triassic boundary in South China. *Science* 289:432–436.
4. Knoll AH, Bambach RK, Payne JL, Pruss S, Fischer WW (2007) Paleophysiology and end-Permian mass extinction. *Earth Planet Sci Lett* 256:295–313.
5. Shen W, Sun Y, Lin Y, Liu D, Chai P (2011) Evidence for wildfire in the Meishan section and implications for Permian–Triassic events. *Geochim Cosmochim Acta* 75: 1992–2006.
6. Joachimski MM, et al. (2012) Climate warming in the latest Permian and the Permian-Triassic mass extinction. *Geology* 40:195–198.
7. Payne JL, et al. (2010) Calcium isotope constraints on the end-Permian mass extinction. *Proc Natl Acad Sci USA* 107:8543–8548.
8. Sun Y, et al. (2012) Lethally hot temperatures during the Early Triassic greenhouse. *Science* 338:366–370.
9. Zhang G, et al. (2017) Redox chemistry changes in the Panthalassic Ocean linked to the end-Permian mass extinction and delayed Early Triassic biotic recovery. *Proc Natl Acad Sci USA* 114:1806–1810.
10. Kump LR, Pavlov A, Arthur MA (2005) Massive release of hydrogen sulfide to the surface ocean and atmosphere during intervals of oceanic anoxia. *Geology* 33: 397–400.
11. Renne PR, Black MT, Zichao Z, Richards MA, Basu AR (1995) Synchrony and causal relations between permian-triassic boundary crises and siberian flood volcanism. *Science* 269:1413–1416.
12. Shen Y, et al. (2011) Multiple S-isotopic evidence for episodic shoaling of anoxic water during Late Permian mass extinction. *Nat Commun* 2:210.
13. Sheldon ND (2006) Abrupt chemical weathering increase across the Permian–Triassic boundary. *Palaeogeogr Palaeoclimatol Palaeoecol* 231:315–321.
14. Algeo TJ, Twitchett RJ (2010) Anomalous Early Triassic sediment fluxes due to elevated weathering rates and their biological consequences. *Geology* 38:1023–1026.
15. Song H, et al. (2015) Integrated Sr isotope variations and global environmental changes through the Late Permian to early Late Triassic. *Earth Planet Sci Lett* 424: 140–147.
16. Misra S, Froelich PN (2012) Lithium isotope history of Cenozoic seawater: Changes in silicate weathering and reverse weathering. *Science* 335:818–823.
17. von Strandmann PAE, Jenkyns HC, Woodfine RG (2013) Lithium isotope evidence for enhanced weathering during Oceanic Anoxic Event 2. *Nat Geosci* 6:668–672.
18. von Strandmann PAE, Henderson GM (2015) The Li isotope response to mountain uplift. *Geology* 43:67–70.
19. Edmond JM (1992) Himalayan tectonics, weathering processes, and the strontium isotope record in marine limestones. *Science* 258:1594–1597.
20. Peucker-Ehrenbrink B, Hannigan RE (2000) Effects of black shale weathering on the mobility of rhenium and platinum group elements. *Geology* 28:475–478.
21. Liu X-M, Rudnick RL, McDonough WF, Cummings ML (2013) Influence of chemical weathering on the composition of the continental crust: Insights from Li and Nd isotopes in bauxite profiles developed on Columbia River Basalts. *Geochim Cosmochim Acta* 115:73–91.
22. Kump LR, Brantley SL, Arthur MA (2000) Chemical weathering, atmospheric CO_2, and climate. *Annu Rev Earth Planet Sci* 28:611–667.
23. Yin H, Zhang K, Tong J, Yang Z, Wu S (2001) The global stratotype section and point (GSSP) of the Permian-Triassic boundary. *Episodes* 24:102–114.
24. Yin H, Xie S, Luo G, Algeo TJ, Zhang K (2012) Two episodes of environmental change at the Permian–Triassic boundary of the GSSP section Meishan. *Earth Sci Rev* 115: 163–172.
25. Burgess SD, Bowring S, Shen SZ (2014) High-precision timeline for Earth's most severe extinction. *Proc Natl Acad Sci USA* 111:3316–3321.
26. Baresel B, et al. (2017) Timing of global regression and microbial bloom linked with the Permian-Triassic boundary mass extinction: Implications for driving mechanisms. *Sci Rep* 7:43630.
27. Shen SZ, et al. (2011) Calibrating the end-Permian mass extinction. *Science* 334: 1367–1372.
28. Chan LH, Edmond JM, Thompson G, Gillis K (1992) Lithium isotopic composition of submarine basalts: Implications for the lithium cycle in the oceans. *Earth Planet Sci Lett* 108:151–160.
29. Vigier N, et al. (2008) Quantifying Li isotope fractionation during smectite formation and implications for the Li cycle. *Geochim Cosmochim Acta* 72:780–792.
30. Jeffcoate AB, Elliott T, Thomas A, Bouman C (2004) Precise/small sample size determinations of lithium isotopic compositions of geological reference materials and modern seawater by MC-ICP-MS. *Geostand Geoanal Res* 28:161–172.
31. Marriott CS, Henderson GM, Belshaw NS, Tudhope AW (2004) Temperature dependence of δ^7Li, δ^{44}Ca and Li/Ca during growth of calcium carbonate. *Earth Planet Sci Lett* 222:615–624.
32. Marriott CS, Henderson GM, Crompton R, Staubwasser M, Shaw S (2004) Effect of mineralogy, salinity, and temperature on Li/Ca and Li isotope composition of calcium carbonate. *Chem Geol* 212:5–15.
33. Plank T, Langmuir CH (1998) The chemical composition of subducting sediment and its consequences for the crust and mantle. *Chem Geol* 145:325–394.
34. Bouman C, Elliott T, Vroon PZ (2004) Lithium inputs to subduction zones. *Chem Geol* 212:59–79.
35. Chen ZQ, et al. (2014) Complete biotic and sedimentary records of the Permian-Triassic transition from Meishan section, South China: Ecologically assessing mass extinction and its aftermath. *Earth Sci Rev* 149:67–107.
36. Tomascak PB (2004) Developments in the understanding and application of lithium isotopes in the earth and planetary sciences. *Rev Mineral Geochem* 55:153–195.
37. Erwin DH, Bowring SA, Jin YG (2002) End-Permian mass extinctions: A review. *Geol Soc Am* 363–384.
38. Korte C, Kozur HW, Bruckschen P, Veizer J (2003) Strontium isotope evolution of late permian and triassic seawater. *Geochim Cosmochim Acta* 67:47–62.
39. Martin EE, Macdougall JD (1995) Sr and Nd isotopes at the Permian/Triassic boundary: A record of climate change. *Chem Geol* 125:73–99.
40. Dellinger M, et al. (2015) Riverine Li isotope fractionation in the Amazon River basin controlled by the weathering regimes. *Geochim Cosmochim Acta* 164:71–93.
41. Svensen H, et al. (2009) Siberian gas venting and the end-Permian environmental crisis. *Earth Planet Sci Lett* 277:490–500.
42. Reichow MK, et al. (2009) The timing and extent of the eruption of the Siberian Traps large igneous province: Implications for the end-Permian environmental crisis. *Earth Planet Sci Lett* 277:9–20.
43. Ivanov AV, et al. (2013) Siberian Traps large igneous province: Evidence for two flood basalt pulses around the Permo-Triassic boundary and in the Middle Triassic, and contemporaneous granitic magmatism. *Earth Sci Rev* 122:58–76.
44. Sobolev SV, et al. (2011) Linking mantle plumes, large igneous provinces and environmental catastrophes. *Nature* 477:312–316.
45. Maruoka T, Koeberl C, Hancox PJ, Reimold WU (2003) Sulfur geochemistry across a terrestrial Permian–Triassic boundary section in the Karoo basin, South Africa. *Earth Planet Sci Lett* 206:101–117.
46. Burgess SD, Bowring SA (2015) High-precision geochronology confirms voluminous magmatism before, during, and after Earth's most severe extinction. *Sci Adv* 1: e1500470.
47. Madison AS, Tebo BM, Mucci A, Sundby B, Luther GW, 3rd (2013) Abundant porewater Mn(III) is a major component of the sedimentary redox system. *Science* 341: 875–878.
48. Gao Y, Casey JF (2012) Lithium isotope composition of ultramafic geological reference materials JP-1 and DTS-2. *Geostand Geoanal Res* 36:75–81.
49. Flesch GD, Anderson AR, Jr, Svec HJ (1973) A secondary isotopic standard for ^{6}Li/^{7}Li determinations. *Int J Mass Spectrom Ion Phys* 12:265–272.
50. Sun H, Gao Y, Xiao Y, Gu HO, Casey JF (2016) Lithium isotope fractionation during incongruent melting: Constraints from post-collisional leucogranite and residual enclaves from Bengbu uplift, China. *Chem Geol* 439:71–82.